

Northumbria Research Link

Citation: Zhao, Long, Wen, Ming, Tian, Yakun, Wu, Qingsheng and Fu, Yong Qing (2022) A novel structure of quasi-monolayered NiCo-bimetal-phosphide for superior electrochemical performance. Journal of Energy Chemistry. ISSN 2095-4956

Published by: Elsevier

URL: <https://doi.org/10.1016/j.jechem.2022.07.017>
<<https://doi.org/10.1016/j.jechem.2022.07.017>>

This version was downloaded from Northumbria Research Link:
<https://nrl.northumbria.ac.uk/id/eprint/49691/>

Northumbria University has developed Northumbria Research Link (NRL) to enable users to access the University's research output. Copyright © and moral rights for items on NRL are retained by the individual author(s) and/or other copyright owners. Single copies of full items can be reproduced, displayed or performed, and given to third parties in any format or medium for personal research or study, educational, or not-for-profit purposes without prior permission or charge, provided the authors, title and full bibliographic details are given, as well as a hyperlink and/or URL to the original metadata page. The content must not be changed in any way. Full items must not be sold commercially in any format or medium without formal permission of the copyright holder. The full policy is available online: <http://nrl.northumbria.ac.uk/policies.html>

This document may differ from the final, published version of the research and has been made available online in accordance with publisher policies. To read and/or cite from the published version of the research, please visit the publisher's website (a subscription may be required.)

1 A novel structure of quasi-monolayered NiCo-bimetal-phosphide 2 for superior electrochemical performance

3 Long Zhao^a, Ming Wen^{a,*}, Yakun Tian^a, Qingsheng Wu^a, Yongqing Fu^b

4
5 ^a *School of Chemical Science and Engineering, Shanghai Key Laboratory of Chemical Assessment*
6 *and Sustainability, State Key Laboratory of Pollution Control and Resource Reuse, Tongji*
7 *University, Shanghai 200092, China*

8 ^b *Faculty of Engineering and Environment, Northumbria University, Newcastle upon Tyne, NE1*
9 *8ST, UK*

10 * Corresponding author. E-mail addresses: m_wen@tongji.edu.cn (M. Wen)

11

12 **Abstract**

13 Bimetallic transition metal phosphides (TMPs) as potential candidates for superior
14 electrochemical performance are still facing great challenges in the controllable preparation of two-
15 dimensional (2D) structures with high aspect ratio. Herein, a novel structure of quasi-monolayered
16 NiCo-bimetal-phosphide (NiCoP) has been designed and successfully synthesized by the newly
17 developed process combined with ultrasonic-cavitation and phase-transition. This is the first time
18 to break through the controllable preparation of 2D bimetal-phosphides with a thickness of 0.98
19 nm in sub-nanoscale. Based on the advantages of 2D quasi-monolayer structure with dense
20 crystalline-amorphous interface and the reconfigured electronic structure between Ni^{δ+}/Co^{δ+} and
21 P^{δ-}, the optimized Ni_{5%}CoP exhibits an outstanding bifunctional performance for electrocatalyzing
22 both hydrogen evolution reaction and oxygen evolution reaction in an alkaline medium. Ni_{5%}CoP
23 presents lower overpotentials and voltage of 84 mV & 259 mV and 1.48 V at the current density
24 of 10 mA·cm⁻² for HER & OER and overall water splitting, respectively, which are superior to
25 most other reported 2D bimetal-phosphides. This work provides a new strategy to optimize the
26 performance of electrolytic water for bimetal-phosphates and it may be of significant value in
27 extending the design of other ultrathin 2D structured catalysts.

28

29 *Keywords:* 2D quasi-monolayer; Hydrogen evolution reaction; Bimetal phosphide; Oxygen
30 evolution reaction; Ultrasonic-cavitation

31

32 **1. Introduction**

33 Hydrogen production by electrolytic water splitting has been regarded as one of ways for
34 generation of green energy [1]. However, both the hydrogen evolution reaction (HER) at cathode
35 and oxygen evolution reaction (OER) at anode require scarce noble metal to meet high
36 electrochemical catalysis performance and superior stability [2]. In order to design and fabricate
37 efficient non-noble-metal based catalysts for bifunctional overall water splitting, abundant 3d
38 transition metal (Co, Ni, Fe, Mn, V, etc.) alloys and their chalcogenides, carbides, nitrides,
39 phosphides have been widely explored [3]. Among them, transition metal phosphides (TMPs) have
40 attracted special attention due to the high catalytic activity of bifunctional overall water splitting
41 derived from their hydrogenase-like catalytic mechanism [4,5], which benefits from unique
42 charging properties of TMPs (positive and negative charges in metal and phosphorus ($M^{\delta+}$ and $P^{\delta-}$),
43 respectively). $M^{\delta+}$ & $P^{\delta-}$ function as proton-acceptor sites & hydride-acceptor sites and coexist on
44 the catalytic crystal surface, which so-called “ensemble effect” that would facilitate overall water
45 splitting [4]. The TMPs are essentially an interstitial compound. The P atoms entering the lattice
46 of the transition metal will increase the spacing between the metal atoms compared with that in the
47 pure phase metal, which will weaken the interaction between the atoms and shrink the d-band of
48 the corresponding transition metal, thus results in an increase in the density of states near the Fermi
49 level (*i.e.* the energy level density of TMPs) compared with the transition metal monomer [6]. This
50 endows TMPs with superior catalytic properties similar to noble metals. In addition, bimetallic
51 phosphates show much better properties than the corresponding monometallic ones [7]. The
52 number of redox centers and conductivity of bimetallic phosphates were significantly improved
53 when the second metal was introduced into the monometallic phosphides [8,9]. More importantly,
54 this process does not change the crystal structure of monometallic phosphides [8]. At the same
55 time, lattice defects or tensile/compression strains caused by the introduction of a second metal or
56 heterostructure/stacking faults during the formation of bimetallic phosphides greatly improves the
57 electrochemical intrinsic activity [10].

58 An ideal electrochemical catalyst for overall water splitting should have the following
59 outstanding characteristics, the maximum exposure of active sites caused by nano-scale, the
60 improvement of catalytic activity per geometric area caused by high aspect ratio, the enhancement
61 of reactants and products mass transfer caused by porous structure [11], the promotion of electron
62 transfer caused by good conductivity, and the improvement of internal catalysis caused by unique
63 physical and chemical properties [12,13]. However, for TMPs with crystal structure of trigonal

64 prisms, controllable synthesis of two-dimensional (2D) structure of porous structure with high
65 aspect ratio in nano scale is a huge challenge [14,15], let alone sub-nanometer level. In recent years,
66 high-intensity ultrasound method, with its advantages of simplicity, efficiency, and cost-
67 effectiveness, provides an effective synthetic strategy for nanomaterials [16]. Ultrasound waves
68 promote the mass transfer between the liquid-solid interfaces. Shock waves (60 kPa) and micro jets
69 (4 km s^{-1}) generated by ultrasound could accelerate the prime particles to high velocities. The
70 collision of these powerful particles leads to their effective fusion, i.e., resulting in ultrasound
71 induced aggregation [17]. Therefore, ultrasound method could be a suitable way to construct 2D
72 nanostructure. However, this technique has never been used for synthesis of 2D TMPs with a sub-
73 nanometer thickness as the effective electrocatalyst toward water splitting.

74 In this work, a novel 2D sub-nanostructure of quasi-monolayered NiCo-bimetal-phosphide
75 (NiCoP) has been successfully synthesized using a strategy cooperated ultrasonic-cavitation with
76 phase-transition (UC-PT). When it is used as HER catalyst for electrolytic water splitting, the $\text{P}^{\delta-}$
77 not only act as proton hydrogen acceptor sites, but also reduce the free energy of adsorbed hydrogen
78 (H^*) on the $\text{Ni}^{\delta+}/\text{Co}^{\delta+}$ active sites. This accelerates the H^* desorption process. Simultaneously,
79 OER activity can also be improved through the formation of NiCoP@NiCoPO_x core-shell
80 structures under an OER overpotential. Besides, the formed abundant and dense crystalline-
81 amorphous (c-a) interfaces provide the suitable crystallinity to balance conductivity and
82 electrocatalytic activity, which have been explained by establishing mathematical models. Thus,
83 Ni_{5%}CoP only needs lower overpotentials and voltage of 84 mV&259 mV and 1.48 V to achieve
84 the current density of $10 \text{ mA}\cdot\text{cm}^{-2}$ for HER&OER and overall water splitting which can maintain
85 for 12 h. Further, it realizes a large current density of $267 \text{ mA}\cdot\text{cm}^{-2}$ at 1.80 V for overall water
86 splitting, which can meet the basic requirements of commercial catalysts for electrolytic water and
87 provide an important guarantee for further commercialization attempts.

88 **2. Experimental section**

89 *2.1. Materials and reagents.*

90 Cobalt chloride hexahydrate ($\text{CoCl}_2\cdot 6\text{H}_2\text{O}$, 98%), nickel chloride hexahydrate ($\text{NiCl}_2\cdot 6\text{H}_2\text{O}$,
91 98%), sodium borohydride (NaBH_4 , 98%), sodium hydride (NaH , 60% dispersion in mineral oil),
92 sodium hydroxide (NaOH , 98%), sodium hypophosphite monohydrate ($\text{NaH}_2\text{PO}_2\cdot 6\text{H}_2\text{O}$, 99%),
93 20% PtC, RuO_2 , and ethanol were obtained from Aladdin Biochemical Technology Co., Ltd.
94 (Shanghai, China).

95 *2.2. The preparation of CoP and NiCoP.*

96 $\text{CoCl}_2 \cdot 6\text{H}_2\text{O}$ (83.3 mg) was dissolved in deionized water (100 mL). Then, 60 mL of this prepared
97 solution was mixed dropwise with a freshly prepared NaBH_4 solution (13 mM, 30 mL) under
98 ultrasonic agitation. After 120 min of reaction, the product of $\text{Co}(\text{OH})_2$ was collected by
99 centrifugation and washed by ethanol and water several times. It was then dried in a freeze drier.
100 Two quartz crucibles were put into a tubular furnace. One was loaded with NaH_2PO_2 (1.8 g) and
101 placed on the upwind side. The other one was loaded with $\text{Co}(\text{OH})_2$ (12 mg) and placed at the
102 downwind side. They were heated up to 350°C (with a heating rate of $2^\circ\text{C} \cdot \text{min}^{-1}$) and kept for 3 h
103 at 350°C for a complete phosphorization. NiCoP were synthesized by a similar protocol of the CoP,
104 except that the starting solutions have dissolved $\text{CoCl}_2 \cdot 6\text{H}_2\text{O}$ (83.3 mg dissolved in 100 mL
105 deionized water, 30 mL) plus $\text{NiCl}_2 \cdot 6\text{H}_2\text{O}$ solution (4.2 mg dissolved in 100 mL deionized water,
106 30 mL).

107 2.3. Characterization.

108 Surface morphologies, thicknesses, and crystal lattice spacings of samples were observed using
109 a scanning electron microscope (SEM, HITACHIS-4800, Japan), an atomic force microscope
110 (AFM, Multimode Nanoscope VIII, America), and a high-resolution transmission electron
111 microscope (HR-TEM, JEM-2100, Japan). Elemental information of samples was obtained using
112 an energy-dispersive X-ray spectroscopy (EDS) at 20 keV. X-ray diffraction patterns were obtained
113 using an X-ray diffractometer (XRD, D/max-RB, Germany) with a $\text{Cu } K\alpha$ radiation source ($\gamma =$
114 0.154056 nm) at $2\theta = 10\text{-}80^\circ$ with the scanning rate of $0.05^\circ/\text{s}$. Chemical elements and their
115 bonding information were obtained using an X-ray photoelectron spectroscope (XPS, PHI-5000C
116 ESCA, America) with $\text{Al } K\alpha$ radiation ($h\nu = 1486.6 \text{ eV}$) on an inVia (Renishaw, U.K.) with He-
117 Ne laser at $\lambda = 514 \text{ nm}$ and a power of 10 to 20 mW. Surface areas were measured using the
118 Brunauer-Emmett-Teller (BET, Micromeritics TRISTAR 3020) method at a relative pressure P/P_0
119 from 0.05 to 0.25. The *in situ* Raman spectra of $\text{Ni}_{5\%}\text{CoP}$ were obtained using a Renishaw inVia
120 with *in situ* test electrolytic cell of Gaoss Union C031-2 at the wavelength of 532 nm.

121 2.4 Electrochemical measurements.

122 Electrochemical performance of the as-prepared materials was measured using an
123 electrochemical workstation (CHI 760E, Shanghai Chenhua). The standard three-electrode setup
124 was composed of a counter electrode (graphite rod, Alfa Aesar, 99.9995%), a reference electrode
125 (Ag/AgCl , 3 M KCl solution), and a working electrode (as-prepared samples were coated on glassy
126 carbon electrode (GCE)). The Ag/AgCl was calibrated to a reversible hydrogen electrode (RHE)
127 based on the Eq. 1:

$$E_{(\text{RHE})} = E_{(\text{Ag}/\text{AgCl})} + E_{(\text{Ag}/\text{AgCl})}^0 + 0.059 \times \text{pH} \quad 1$$

129 The electrode slurries were prepared by sonicating a mixture of catalyst (4 mg), Nafion (10 μL),
 130 and solvent (water/ethanol with volume ratio 3:1, 1 mL) for 30 min until a homogenous dispersion
 131 was formed. The electrode slurries of 10 μL were dropped onto the GCE with a diameter of 3 mm,
 132 which was naturally dried to form a working electrode. Processes of hydrogen evolution reaction
 133 and oxygen evolution reaction were carried out in a 1 M KOH aqueous solution (pH = 14) at
 134 ambient temperature after blowing N_2 and O_2 for 30 min, respectively. Before the data collection,
 135 the activation treatment was implemented via 40 cycles of cyclic voltammetry (CV) in the range
 136 of 0.2 ~ 0.6 V (vs. RHE). Linear sweep voltammetry (LSV) of samples was used to examine the
 137 electrochemical activities and carried out within a range of 0.3 ~ 0.5 V (vs. RHE) and 1.2 ~ 1.7 V
 138 (vs. RHE) at a scan rate of 2 mV s^{-1} for HER and OER, respectively. All the polarization curves
 139 were presented with iR correction. The compensated potential was determined using Eq. 2:

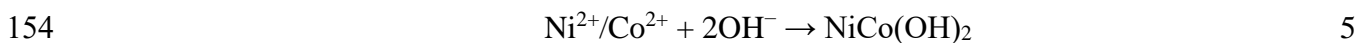
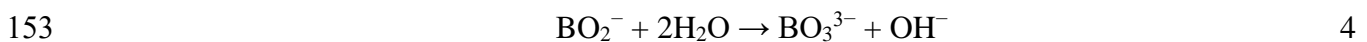
$$E_{\text{compensated}} = E_{\text{measured}} - i \times R_s \quad 2$$

141 where R_s is the series resistance determined by electrochemical impedance spectroscopy (EIS),
 142 which was obtained at an amplitude of 5 mV within a frequency range from 105 to 0.01 Hz. For
 143 the determination of double layer capacitance (C_{dl}), CV scans between 0.2~0.6 V (vs. RHE) were
 144 conducted at scan rates of 20, 40, 60, 80, and 100 mV s^{-1} . Additionally, the long-term stability test
 145 of catalysts was conducted with the applied potential of 90 mV (HER) and 1.5 mV (OER) vs. RHE
 146 for 12 h.

147 3. Results and discussion

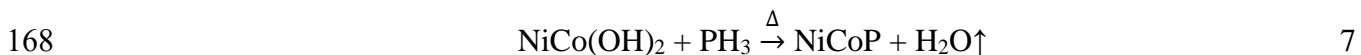
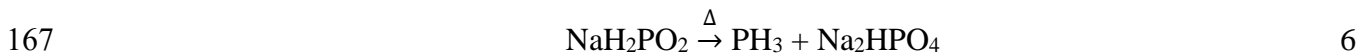
148 3.1 Fabrication and structure.

149 2D quasi-monolayered NiCoP is synthesized through a newly developed UC-PT process, as
 150 illustrated in Fig. 1. In Step 1, OH^- generated from the hydrolysis processes, in which BH_4^+ react
 151 with $\text{Ni}^{2+}/\text{Co}^{2+}$ to form $\text{NiCo}(\text{OH})_2$, according to Eqs. 3-5 [18–20]:

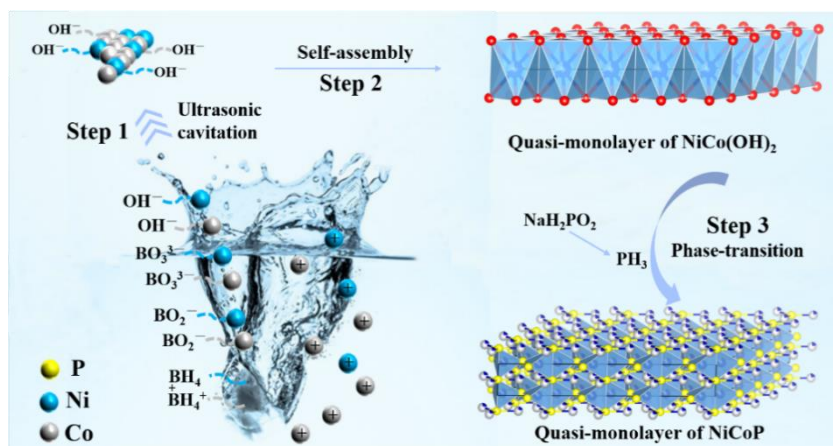


155 To verify the conversion of OH^- from the hydrolysis process of BH_4^+ , the NaH and NaOH were
 156 selected (Fig. S1). Smooth and spherical nanoparticles were obtained when NaBH_4 was replaced
 157 with NaH. If NaOH is used, a mixed morphology of flower sphere, nano particles, and nano sphere
 158 can be observed. These results unambiguously confirm that the involvement of hydroxyl converted
 159 from boron species is crucial in forming the ultrathin $\text{NiCo}(\text{OH})_2$. Meanwhile, cavitation bubbles

160 are generated due to high-frequency oscillations of the ultrasonic waves. When cavitation bubbles
 161 are randomly ruptured, the generated high-speed micro-jets and shock waves effectively promote
 162 self-assembly of NiCo(OH)₂ to form ultrathin quasi-monolayered NiCo(OH)₂ (Step 2) [21]. The
 163 unfolding degree of NiCo(OH)₂ increases with the increase of ultrasonic power (Fig. S2). The
 164 subsequent phosphating process produces 2D quasi-monolayered NiCoP through the synchronous
 165 phase-transition process of NiCo(OH)₂ and the decomposition product PH₃ of NaH₂PO₂ (Step 3,
 166 Eqs. 6-7) [22].



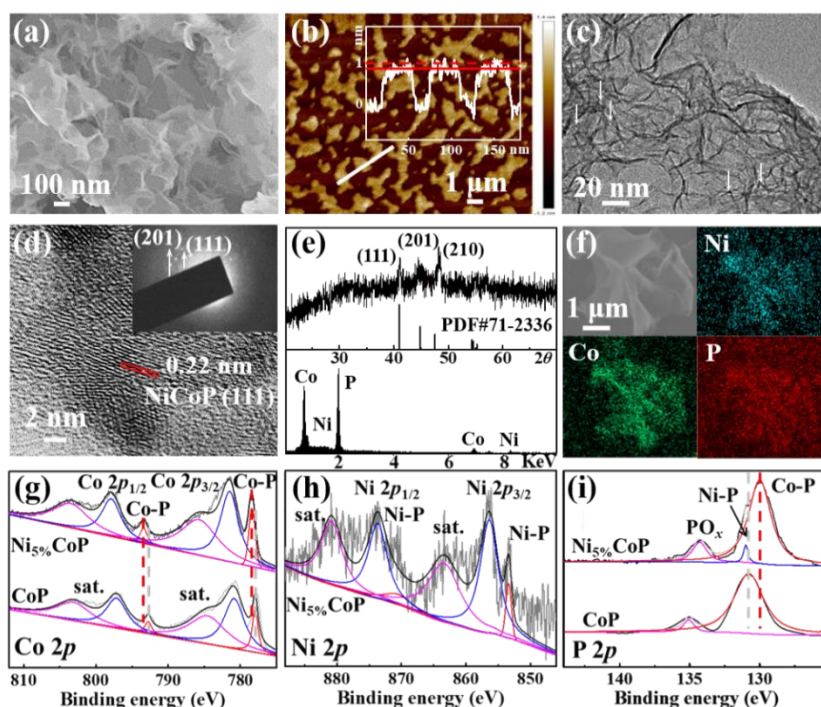
169 (NiCo)₃O₄ will be obtained if there is no phosphorus source, which indirectly proves this process
 170 (Fig. S3, Eq. 8).



172
 173 **Fig. 1.** Synthesis scheme of 2D quasi-monolayered NiCoP by cavitation at the ultrasonic-pulse interface.

174 Fig. 2 shows characterization results for the obtained 2D quasi-monolayered Ni_{5%}CoP under the
 175 optimized synthesis conditions. In Fig. 2(a and b), SEM images reveal 2D sub-nanostructures with
 176 a thickness of 0.98 nm. Abundant mesopores can be observed from TEM image (Fig. 2c). The
 177 estimated surface area is ~110.74 m²·g⁻¹ and the average pore diameter is 5 nm, which was obtained
 178 by BET measurement (Fig. S4). Such structures can create abundant edges and expose numerous
 179 active sites, both of which are highly beneficial for the kinetic process toward electrocatalytic water
 180 splitting. HR-TEM image (Fig. 2d) shows a fringe spacing of 0.22 nm, corresponding to the (111)
 181 facet of Ni_{5%}CoP. Apparent c-a interfaces are observed in Fig. S5, where the crystalline phase
 182 promotes the electron transfer and the amorphous phase with abundant unsaturated coordination

183 sites provides plentiful adsorption sites of intermediates [23]. Meanwhile, the c-a interfaces can
 184 modulate the electron structure of Ni_{5%}CoP and optimize the adsorption/desorption of
 185 intermediates, thus promoting the electrocatalytic performance of both HER and OER for
 186 electrolytic water splitting [24]. The selected area diffraction (SAED) pattern of the 2D quasi-
 187 monolayered Ni_{5%}CoP presents its (111) and (201) plane facets (Inset of Fig. 2d), which are also
 188 confirmed by XRD pattern (Fig. 2e above). It reveals the diffraction peaks at 40.99°, 44.90°,
 189 47.58°, 54.44°, 54.74°, and 55.33°, which are respectively corresponding to (111), (201), (210),
 190 (300), (002), and (211) lattice planes of hexagonal NiCoP (PDF#: 71-2336). EDS (Fig. 2e below)
 191 and elemental mapping (Fig. 2f) reveal the uniform distribution of Co, Ni, and P. This clearly
 192 reveals that the obtained Ni_{5%}CoP crystals have a lattice integrated with Ni/Co hetero-metal co-site
 193 atoms, owing to the similar atom radii of both Ni and Co [25].



194
 195 **Fig. 2.** SEM (a), AFM (b), TEM (c), HR-TEM (SAED pattern illustration) (d), XRD pattern (above) and EDS
 196 spectra (below) (e), mapping images (f) of Ni_{5%}CoP. Detail XPS spectra for Co 2p, P 2p, and Ni 2p of CoP and
 197 Ni_{5%}CoP (g-i).

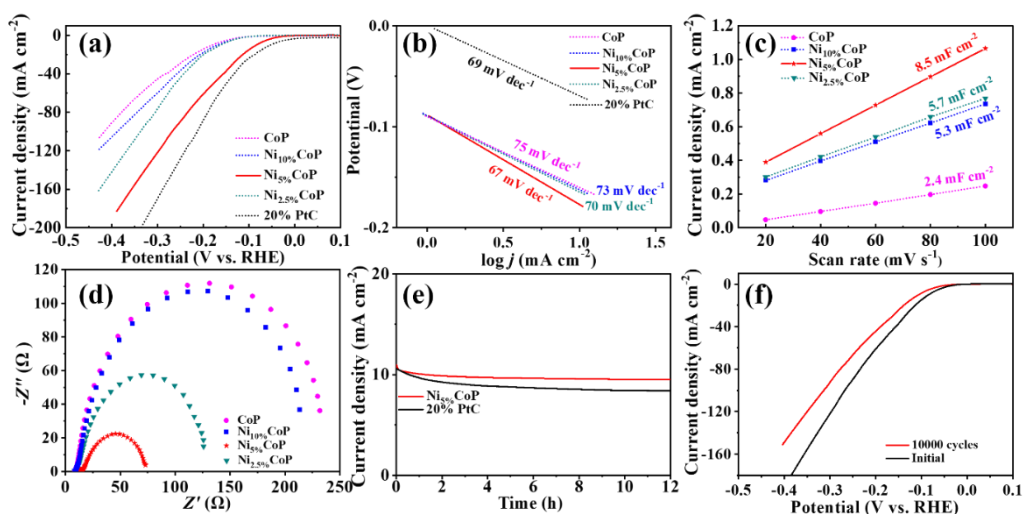
198 Survey spectra of XPS for Ni_{5%}CoP and CoP were obtained to investigate their chemical states
 199 of different elements (Fig. S6). The survey spectrum of Ni_{5%}CoP reveals the existence of Co, Ni,
 200 and P, while Ni is absent in the survey spectrum of CoP. High resolution spectra of Co 2p for both
 201 the Ni_{5%}CoP and CoP exhibit two regions (Fig. 2g). Peaks at 781.58 eV are attributed to Co 2p_{3/2},
 202 while the peak at 785.98 eV belongs to the satellite peak of Co 2p_{3/2}. The Co 2p_{1/2} region also

203 exhibits two main peaks at 797.98 eV and one satellite peak at 803.78 eV [26]. The above spin-
204 orbit doublets could be ascribed to oxidized states of Co species, which may be due to the
205 superficial oxidation of Ni_{5%}CoP [27]. For peaks of 778.28 and 793.38 eV are assigned to the cobalt
206 phosphide (Co-P) bond [28]. This binding energy is also found to be slightly higher than that of
207 metallic Co (778.2 eV) [29], indicating that the Co carries a partially positive charge (Co^{δ+}, δ is
208 likely to close to 0) in Ni_{5%}CoP [30]. Similarly, peaks at 853.38 eV and 870.58 eV in the Ni 2p
209 region are observed (Fig. 2h) [31], suggesting the presence of partially charged Ni species (Ni^{δ+})
210 derived from Ni-P compounds in Ni_{5%}CoP. Note that the binding energy of 853.38 eV is also close
211 to that of metallic Ni (852.6 eV) [32]. The signals at 856.58 eV (2p_{3/2}) and 873.88 eV (2p_{1/2}) with
212 their satellite peaks at 863.38 and 880.98 eV are assigned to oxidized states of Ni species [31]. In
213 Fig. 2(i), three peaks corresponding to P 2p are noted. The peak attributed to phosphate (NiCoPO_x)
214 at 134.28 eV is caused by the superficial oxidation of Ni_{5%}CoP after exposure to air [27]. Peaks of
215 130.88 eV and 129.98 eV are assigned to P bonded with Ni or Co (Ni-P or Co-P), respectively
216 [33]. It is worth noting that compared with Co(0) (778.2 eV), Ni(0) (852.6 eV), and P(0) (130.2
217 eV), Ni and Co in Ni_{5%}CoP have partly positive charge (δ⁺) shifts, while P shows a negative charge
218 (δ⁻) shift. This result indicates the low electron density transfer from Ni and Co to P, due to the
219 much stronger transfer of P than Ni and Co, which exacerbates the polarization of electrons [34].
220 Besides, it was reported that the local electric dipoles produced by Ni, Co, and P can reduce the
221 energy barrier of the catalytic process and increase the catalytic activity [35]. In general, the
222 sluggish kinetics of the overall water splitting under an alkaline condition could be caused by two
223 reasons. The first one is that the transport rate of OH⁻ is lower than that of H⁺ in an alkaline
224 electrolyte solution. The other one is due to the increased difficulty for the cleavage of HO-H bonds
225 in water molecules than that in the hydrated protons [36]. For the above two points, the capture of
226 H⁺ by P^{δ-} and the adsorption of OH⁻ by the unfilled d-orbitals of Ni^{δ+}/Co^{δ+} result in the Ni_{5%}CoP
227 effectively catalyzes the cleavage of HO-H bonds [37]. The generated H* are further transferred to
228 the adjacent active Ni^{δ+}/Co^{δ+} sites. The continuous dissociation and transfer of H* accelerate the
229 Volmer-Heyrosky process [38].

230 3.2. Evaluation of electrocatalytic activity.

231 In order to accurately evaluate intrinsic activity, the electrode slurries containing synthesized 2D
232 quasi-monolayered NiCoP were prepared and directly coated onto the surface of GCE to study its
233 electrocatalytic performance in a 1 M KOH solution. For the HER process, Fig. 3(a) plots the
234 polarization curves of the LSV. Ni_{5%}CoP shows a low overpotential at the current density of 10

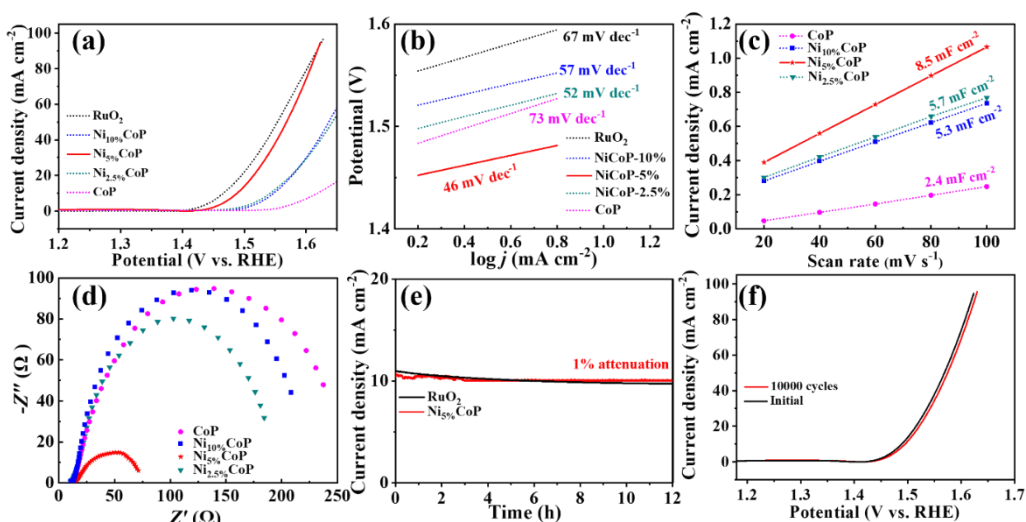
235 $\text{mA}\cdot\text{cm}^{-2}$ (η_{10}) of 84 mV which surpasses the precursor of $\text{Ni}_{5\%}\text{Co}(\text{OH})_2$ (Fig. S7) and compared
 236 materials of $\text{Ni}_{2.5\%}\text{CoP}$, $\text{Ni}_{10\%}\text{CoP}$, CoP , and $(\text{NiCo})_3\text{O}_4$. The overpotential of $\text{Ni}_{5\%}\text{CoP}$ is also
 237 superior to most other reported TMPs (Table S1). The $\text{Ni}_{5\%}\text{CoP}$ achieves large current densities of
 238 $180 \text{ mA}\cdot\text{cm}^{-2}$ at an overpotential of 390 mV, which is much larger than that of $\text{Ni}_{2.5\%}\text{CoP}$,
 239 $\text{Ni}_{10\%}\text{CoP}$, and CoP . The Tafel slopes of $\text{Ni}_{2.5\%}\text{CoP}$, $\text{Ni}_{5\%}\text{CoP}$, $\text{Ni}_{10\%}\text{CoP}$, and CoP are 70, 67, 73,
 240 and $75 \text{ mV}\cdot\text{dec}^{-1}$ (Fig. 3b and Fig. S8, Table S2), which are all within range of $40\text{-}120 \text{ mV}\cdot\text{dec}^{-1}$.
 241 This means that they all follow the Volmer-Heyrovsky mechanism [39]. The lowest Tafel slopes
 242 of $\text{Ni}_{5\%}\text{CoP}$ indicate that the catalysis can be enhanced *via* the optimization of Ni/Co hetero-metal
 243 co-site atoms. To further understand the HER performance, electrochemically active surface area
 244 (ECSA) was estimated from the data of C_{dl} using a CV method (Fig. 3c and Fig. S9a). $\text{Ni}_{5\%}\text{CoP}$
 245 exhibits the highest C_{dl} value at $17.3 \text{ mF}\cdot\text{cm}^{-2}$, which is 1.17, 1.80, and 5.41 times higher than
 246 those of $\text{Ni}_{2.5\%}\text{CoP}$, $\text{Ni}_{10\%}\text{CoP}$ and CoP , respectively. The EIS measurements demonstrate that the
 247 lowest charge transfer resistance of $\text{Ni}_{5\%}\text{CoP}$ is deduced by the smallest semicircular diameter (Fig.
 248 3d). For the excellent stability of $\text{Ni}_{5\%}\text{CoP}$, the initial current density of $10 \text{ mA}\cdot\text{cm}^{-2}$ at an
 249 overpotential of 84 mV was only attenuated by 13% after 12 h of chronopotentiometry, which is
 250 better than the commercial 20% Pt/C (Fig. 3e). In addition, the minor attenuation of LSV curves
 251 after 10000 CV cycles further confirms the good stability of $\text{Ni}_{5\%}\text{CoP}$ (Fig. 3f).



252
 253 **Fig. 3.** LSV polarization curves (a), Tafel slope (b), dependence of capacitive current on scan rates (c), Nyquist
 254 plots (d), stability tested using chronopotentiometry (e), LSV polarization curves before and after 10000 cycles
 255 (f) for HER.

256 As it is well known, OER is the rate-determining step of overall water splitting. Therefore, the
 257 OER performance of the NiCoP samples in a 1 M KOH solution was tested. $\text{Ni}_{5\%}\text{CoP}$ presents the
 258 smallest overpotential of 259 mV to achieve a current density of $10 \text{ mA}\cdot\text{cm}^{-2}$ (Fig. 4a). This value

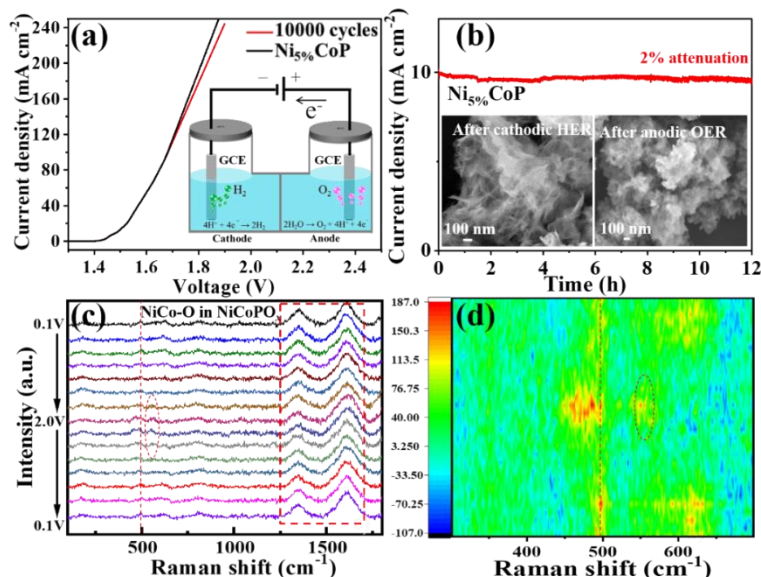
259 is superior to those of comparison samples ($\eta_{10} = 230, 312, 318,$ and 389 mV for $\text{RuO}_2, \text{Ni}_{2.5\%}\text{CoP},$
 260 $\text{Ni}_{10\%}\text{CoP},$ and CoP) and most other reported TMPs (Table S3). As shown in Fig. 4(b), the Tafel
 261 slopes are $52, 46,$ and 57 $\text{mV}\cdot\text{dec}^{-1}$ for the $\text{Ni}_{2.5\%}\text{CoP}, \text{Ni}_{5\%}\text{CoP},$ and $\text{Ni}_{10\%}\text{CoP}$ samples, all of
 262 which are lower than that for CoP (73 $\text{mV}\cdot\text{dec}^{-1}$). This is mainly because Ni/Co hetero-metal co-
 263 site atoms reduce the oxygen affinity of Co atoms [40]. In addition, $\text{Ni}_{5\%}\text{CoP}$ has shown the highest
 264 C_{dl} value and the smallest semicircular diameter, which enables it to achieve the largest current
 265 density at the smallest overpotential than those of the other comparison samples (Fig. 4c-d and Fig.
 266 S9b). The good stability and durability of $\text{Ni}_{5\%}\text{CoP}$ can be revealed from the stable current density
 267 of 10 $\text{mA}\cdot\text{cm}^{-2}$ of 12 h (1% attenuation), which is tested by a chronopotentiometry test at a static
 268 overpotential of 259 mV. The value is nearly equivalent to that of RuO_2 (Fig. 4e). Meanwhile, there
 269 are no apparent decays of performance after 10000 CV cycles in the LSV curves (Fig. 4f).



270
 271 **Fig. 4.** LSV polarization curves (a), Tafel slope (b), dependence of capacitive current on scan rates (c), Nyquist
 272 plots (d), stability tested using chronopotentiometry (e), LSV polarization curves before and after 10000 cycles
 273 (f) for OER.

274 The excellent performance for the HER and OER half-reactions suggests that $\text{Ni}_{5\%}\text{CoP}$ has the
 275 potential for commercial electrolytic water splitting applications. Thus, the obtained $\text{Ni}_{5\%}\text{CoP}$ was
 276 applied as both the anode and cathode working electrodes for overall water splitting (Inset of Fig.
 277 5a). When the overpotentials were 1.48 and 1.80 V, the current densities of 10 and 267 $\text{mA}\cdot\text{cm}^{-2}$
 278 can be obtained, respectively (Fig. 5a). These values can be able to meet the requirements of
 279 commercial catalysts for electrolytic water ($1.8 \sim 2.4$ V up to $200 \sim 400$ $\text{mA}\cdot\text{cm}^{-2}$). As far as we
 280 know, these values cannot be achieved by simply using the other TMPs. Moreover, the LSV curves
 281 did not show apparent decay after 10000 cycles (Fig. 5a). The stable current density and

282 morphology can also be maintained after chronoamperometry for 12 h, revealing excellent
 283 durability (Fig. 5b and illustration). It is worth noting the XPS result of Ni_{5%}CoP on the anode
 284 reveals that the PO_x peak in high resolution spectra of P 2*p* is significantly enhanced after OER
 285 (Fig. S10). It is because more Ni_{5%}CoP on the surface forms NiCoP@NiCoPO_x core-shell structure
 286 through the initial oxidation reaction, where the NiCoP core provides an effective electron transfer
 287 pathway and the NiCoPO_x shell acts as an active site for OER [41]. In order to identify the changes
 288 of intermediate species and stability of Ni_{5%}CoP during OER process, a potential-dependent *in situ*
 289 Raman analysis was performed (Fig. 5c and d). At a voltage low than 1.3 V, the *in situ* Raman
 290 spectra show a weak peak at 497 cm⁻¹ which can be assigned to e_g bending vibration of NiCoP-O
 291 in NiCoPO_x [42]. With increasing the voltage to 1.5 V, the characteristic peak at 525 cm⁻¹, which
 292 corresponds to the A_{1g} stretching vibration of NiCoP-O in NiCoPO_x [43], is gradually increased
 293 afterward with the increase of bending vibration. It is quite interesting to see that the self-
 294 reconstruction of NiCoP-O in NiCoPO_x is reversible during reverse scanning, and only a small
 295 peak is detected after OER. Moreover, the original characteristic peaks at 1349 and 1606 cm⁻¹ in
 296 the *in situ* Raman spectra show no clear changes after OER (Fig. S11). The stable phase structure
 297 endows the Ni_{5%}CoP with efficient electrocatalytic activity and high stability for OER.



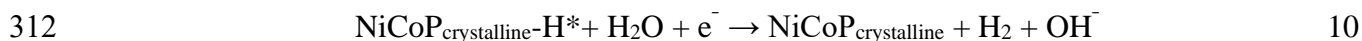
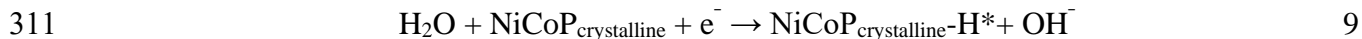
298 **Fig. 5.** LSV polarization curves before and after 10000 CV cycles (a), stability by chronopotentiometry (b) during
 299 overall water splitting process. *In situ* Raman and contour map spectra (c and d) of Ni_{5%}CoP during OER process.
 300

301 3.3. Discussion.

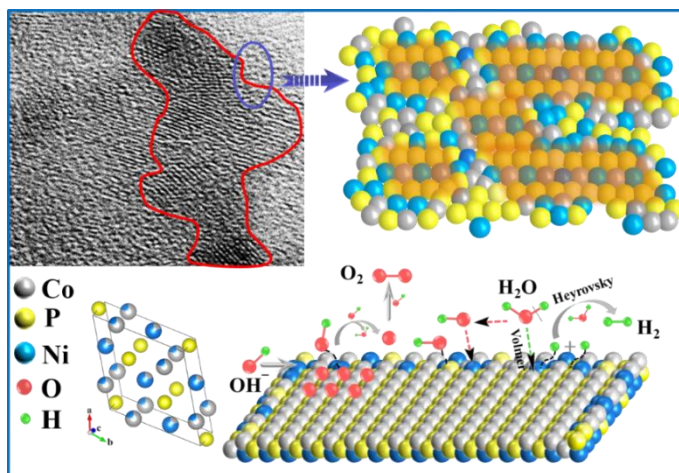
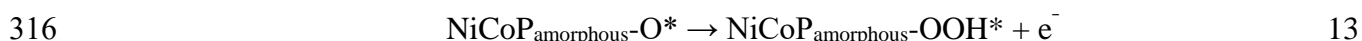
302 In the alkaline electrolyte water splitting, the degradation of catalytic activity of TMPs is often
 303 caused by the decreased areas of the active electrode due to the generated gas bubbles which are

304 covered on the electrode surface [44]. This problem can be solved *via* the obtained dense c-a
 305 interface structure (Fig. 6 above). The long-range disorder structure of the amorphous phase leads
 306 to the formation of randomly-oriented bonds of internal atoms, resulting in many numbers of
 307 coordination unsaturated sites [45]. The HO-H bond splitting process can occur at the c-a interfaces
 308 through the adsorption of the amorphous region for OH⁻ and the crystalline region for H⁺ (Fig. 6
 309 below). The reaction of HER and OER process is as follows:

310 HER process:



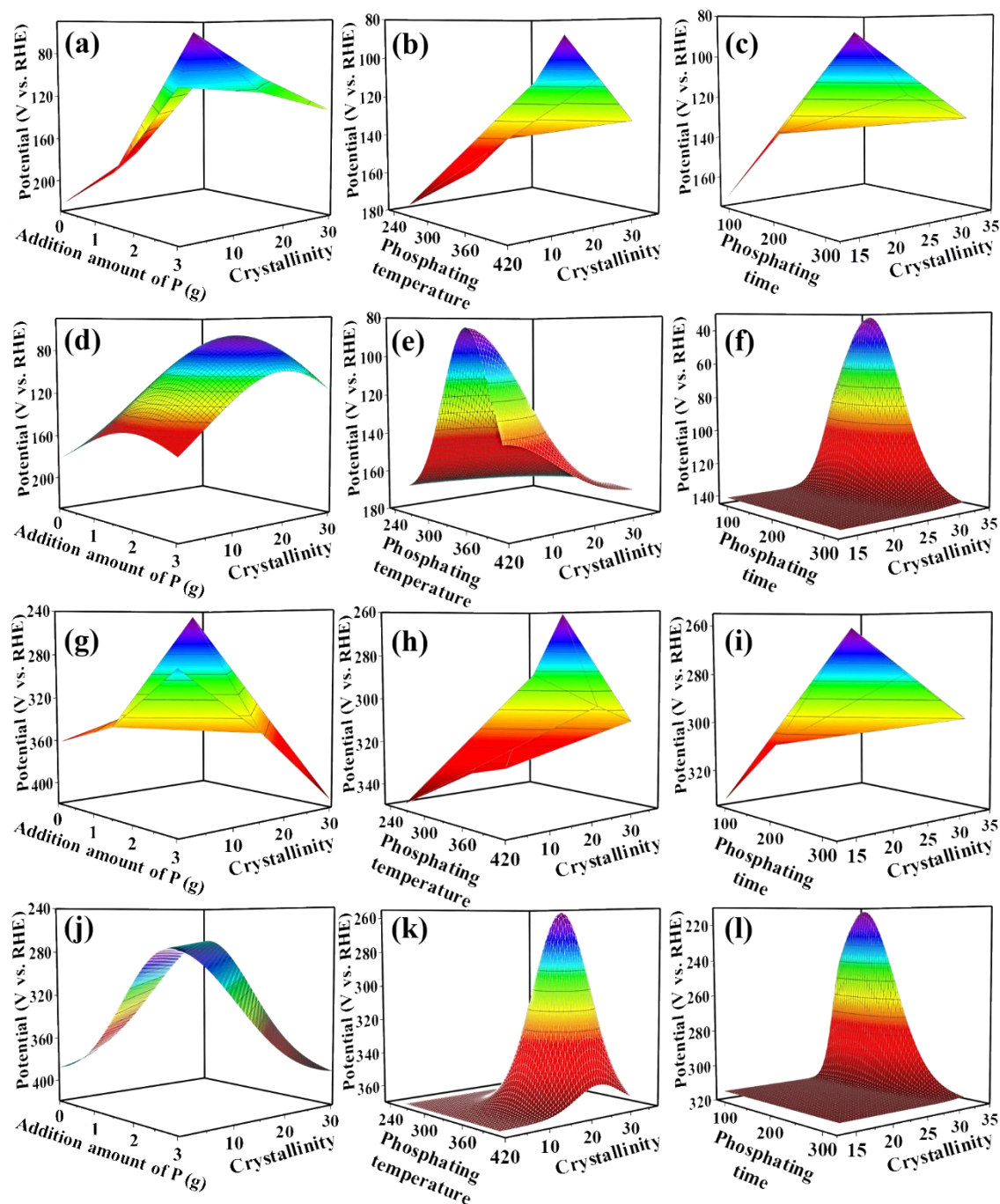
313 OER process:



318
 319 **Fig. 6.** Catalytic mechanism diagram for overall water splitting at crystalline-amorphous phase interfaces

320 It should be addressed that a fully amorphous catalyst shows very low conductivity whereas the
 321 crystalline phase can achieve a high conductivity by promoting electron transfer [46]. Therefore, a
 322 suitable crystallinity of c-a interface can not only ensure the conductivity of Ni_{5%}CoP, also improve
 323 the desorption process of the generated gas in the crystalline region. On the other hand, the
 324 crystallinity of TMPs also has an important influence on its conductivity. This is because the
 325 different proportions of P/M will change the electronic structure, which essentially changes its
 326 electrocatalytic activity. Too high phosphorus content in TMPs will reduce the number of free
 327 electrons in the material, resulting in a significant decrease in conductivity, so that the catalytic

328 performance reduces [15]. Similarly, the phosphating process is controlled by the thermodynamics
 329 and kinetics of reaction temperature and time, they also have an important influence on the relative
 330 crystallinity. Researchers pay much attention to the preparation methods and electrochemical
 331 properties of catalyzers, but pay little attention to the effect of crystallinity on the electrocatalytic
 332 properties.



333
 334 **Fig. 7.** 3D variation trend and Gaussian fitting diagrams of HER (a-c) & (d-f) and OER (g-i) & (j-l) among
 335 crystallinity, overpotential, and phosphating conditions for Ni_{5%}CoP.

336 Therefore, a balance between conductivity and high phosphorus content can be found by
337 adjusting the crystallinity of phosphide. Based on the above theory, the effects on the different
338 amounts of P, phosphating temperature, phosphating time, and relative crystallinity of Ni_{5%}CoP on
339 the properties were investigated in the work. It can be found that the synthesis conditions have no
340 obvious effect on the morphology during the investigation (Fig. S12-Fig. 14), but performances of
341 HER and OER of Ni_{5%}CoP obtained under different synthesis conditions are obviously different
342 and have certain rules (Fig. S15). For HER in this study, the relationships among phosphating
343 conditions, crystallinity, and overpotential for Ni_{5%}CoP are shown in Fig. 7(a-c), respectively.
344 Further, mathematical fitting models are obtained by fitting the change trends using a Gaussian
345 function (Fig. 7d-f):

$$346 \quad Z = a - b \times \exp(c \times ((x - d) \times \cos\theta + (y - e) \times \sin\theta) / f)^2 - g \times ((-x + h) \times \sin\theta + (y - i) \times \cos\theta) / j)^2 \quad 15$$

347 where Z , y and x refer to overpotential at the current density of 10 mA·cm⁻², crystallinity, and
348 phosphating conditions (a - j are constants). Table S4 lists all obtained data from the fitting curves
349 using the Eq. 15.

350 Fig. 7(g-i) show the effects between phosphating conditions and crystallinity on the OER
351 performance of Ni_{5%}CoP. Meanwhile, the corresponding mathematical fitting models are shown in
352 Fig. 7(j-l) (all the parameters used in Eq. 15 are listed in Table S5). All these results prove the
353 superior OER performance at a crystallinity of 30% for the Ni_{5%}CoP. Based on the above
354 information, the (111) crystal surfaces can be exposed more effectively when the crystallinity of
355 Ni_{5%}CoP increases with the increase of phosphating temperature and time. These will lead to
356 enhanced electrocatalytic activity [47]. However, HER performance becomes deteriorated when
357 the phosphating temperature exceeds 350°C or the phosphating time exceeds 3 h, mainly because
358 the agglomeration of 2D structure reduces the number of active sites. It is worthwhile to address
359 that the deterioration of HER performance can also be observed when the amount of P is more than
360 28%. Too high a concentration of P will restrict electron migration of metal and reduce its
361 conductivity, thus inhibiting the activity of electrolytic water splitting. Based on the data in this
362 study, an optimal overpotential of HER could be achieved when the crystallinity is about 30%,
363 suggesting that the ratio between crystalline and amorphous phases can be controlled to balance
364 the conductivity and crystallinity.

365 4. Conclusions

366 In this work, 2D quasi-monolayered NiCoP in subnanosized thickness was fabricated using a
367 newly developed UC-PT process, which appears excellent performance toward electrolytic water

368 splitting due to the following points. i) The quasi-monolayered 2D structure with sub-nanometer
369 thickness exposes more active sites. ii) The reconfigurable electronic structure through polarization
370 between $\text{Ni}^{\delta+}/\text{Co}^{\delta+}$ and $\text{P}^{\delta-}$ to optimize adsorption/desorption energy in HER. NiCo-O active sites
371 in NiCoP@NiCoPO_x core-shell layered structure can enhance OER activity. iii) The c-a interfaces
372 *via* the synergistic effect of crystalline and amorphous phases promote the cleavage of HO-H
373 bonds. The suitable c-a interfaces give full play to the advantages of crystalline and amorphous
374 phases. Based on the established mathematical models, the influences of the relative crystallinity
375 are well discovered for the electrolytic water splitting. This provides a new strategy for the design
376 of bimetallic phosphates with ultrathin 2D structure to catalyze overall water splitting.

377

378 **Declaration of Competing Interest**

379 The authors declare that they have no known competing financial interests or personal
380 relationships that could have appeared to influence the work reported in this paper.

381

382 **Acknowledgments**

383 This work was financially supported by the National Natural Science Foundation (22171212),
384 the Science and Technology Committee of Shanghai Municipality (21160710300, 19DZ2271500)
385 of China, the International Exchange Grant (IEC/NSFC/201078) through Royal Society UK and
386 NSFC.

387

388 **Supporting Information**

389 Additional details of supplementary material are presented: Figures (Figure S1-S15) and Tables
390 (Table S1-S5).

391

392

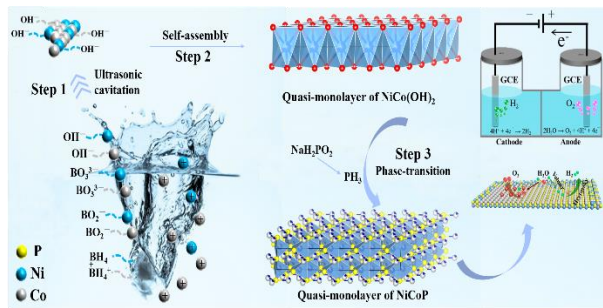
393 **References**

- 394 [1] Y.Q. Feng, R. Wang, P.P. Dong, X. Wang, W.H. Feng, J.S. Chen, L.Y. Cao, L.L. Feng, C.Z.
395 He, J.F. Huang, *ACS Appl. Mater. Interfaces* 13 (2021) 48949-48961.
- 396 [2] S. Shit, S. Bolar, N.C. Murmu, T. Kuila, *J. Energy Chem.* 59 (2021) 160-190.
- 397 [3] Y.Q. Sun, T. Zhang, C.C. Li, K. Xu, Y. Li, *J. Mater. Chem. A* 8 (2020) 13415-13436.
- 398 [4] P. Liu, J.A. Rodriguez, *J. Am. Chem. Soc.* 127 (2005) 14871-14878.
- 399 [5] Y.T. Yan, P.C. Wang, J.H. Lin, J. Cao, J.L. Qi, *J. Energy Chem.* 58 (2021) 446-462.
- 400 [6] Y. Pan, K. Sun, Y. Lin, X. Cao, Y.S. Cheng, S.J. Liu, L.Y. Zeng, W.C. Cheong, D. Zhao, K.L.
401 Wu, Z. Liu, Y.Q. Liu, D.S. Wang, Q. Peng, C. Chen, Y.D. Li, *Nano Energy* 56 (2019) 411-419.
- 402 [7] J. Wang, F. Ciucci, *Appl. Catal. B Environ.* 254 (2019) 292-299.
- 403 [8] G.T. Zan, T. Wu, F. Zhu, P.F. He, Y.P. Cheng, S.S. Chai, Y. Wang, X.F. Huang, W.X. Zhang,
404 Y. Wan, X.J. Peng, Q.S. Wu, *Matter* 4 (2021) 3232-3247.
- 405 [9] H.M. Liu, M.M. Jin, D. Zhan, J.M. Wang, X.Y. Cai, Y.T. Qiu, L.F. Lai, *Appl. Catal. B Environ.*
406 272 (2020) 118951.
- 407 [10] N. Zhang, Y.F. Li, J.Y. Xu, J.J. Li, B. Wei, Y. Ding, I. Amorim, R. Thomas, S.M. Thalluri,
408 Y.T. Liu, G.H. Yu, L.M. Liu, *ACS Nano* 13 (2019) 10612-10621.
- 409 [11] W. Ou, J.Q. Pan, Y.Y. Liu, S. Li, H.L. Li, W.J. Zhao, J.J. Wang, C.S. Song, Y.Y. Zheng, C.R.
410 Li, *J. Energy Chem.* 43 (2020) 188-194.
- 411 [12] G.T. Zan, T. Wu, W.Y. Dong, J.C. Zhou, T. Tu, R.X. Xu, Y. Chen, Y. Wang, Q.S. Wu. *Adv.*
412 *Fiber Mater.* (2022) DOI: 10.1007/s42765-022-00162-7.
- 413 [13] L.F. Xiong, B. Wang, H.R. Cai, H.J. Hao, J. Li, T. Yang, S.C. Yang, *Appl. Catal. B Environ.*
414 295 (2021) 120283.
- 415 [14] G.T. Zan, T. Wu, Z.L. Zhang, J. Li, J.C. Zhou, F. Zhu, H.X. Chen, M. Wen, X.C. Yang, X.J.
416 Peng, J. Chen, Q.S. Wu. *Adv. Sci.* 9 (2022) 2103714.
- 417 [15] Y.M. Shi, B. Zhang, *Chem. Soc. Rev.* 45 (2016) 1529-1541.
- 418 [16] C.L. Yu, J.C. Yu, C.F. Fan, H. Wen, S.J. Hu, *Mater Sci Eng B.* 166 (2010) 213-219.
- 419 [17] C.L. Yu, J.C. Yu, *Mater Sci Eng B.* 164 (2009) 16-22.
- 420 [18] P.Z. Chen, K. Xu, T.P. Zhou, Y. Tong, J.C. Wu, H. Cheng, X.L. Lu, H. Ding, C.Z. Wu, Y.
421 Xie, *Angew. Chem. Int. Ed.* 55 (2016) 2488-2492.
- 422 [19] W.J. Jiang, S. Niu, T. Tang, Q.H. Zhang, X.Z. Liu, Y. Zhang, Y.Y. Chen, J.H. Li, L. Gu, L.J.
423 Wan, J.S. Hu. *Angew. Chem. Int. Ed.* 56 (2017) 6572-6577.

- 424 [20] H. Fan, X. Huang, L. Shang, Y.T. Cao, Y.F. Zhao, L.Z. Wu, C.H. Tung, Y.D. Yin, T.R. Zhang,
425 Angew. Chem. Int. Ed. 55 (2016) 2167-2170.
- 426 [21] L. Qin, B.M. Maciejewska, T. Subroto, J.A. Morton, K. Porfyrakis, I. Tzanakis, D.G. Eskin,
427 N. Grobert, K. Fezzaa, J.W. Mi, Carbon 186 (2022) 227-237.
- 428 [22] Q.X. Guan, W. Li, M.H. Zhang, K.Y. Tao, J. Catal. 263 (2009) 1-3.
- 429 [23] Y.F. Zhao, J.Q. Zhang, Y.H. Xie, B. Sun, J.J. Jiang, W.J. Jiang, S.B. Xi, H.Y. Yang, K. Yan,
430 S.J. Wang, X. Guo, P. Li, Z.J. Han, X.Y. Lu, H. Liu, G.X. Wang, Nano Lett. 21 (2021) 823-
431 832.
- 432 [24] D. Li, Y.Y. Qin, J. Liu, H.Y. Zhao, Z.J. Sun, G.B. Chen, D.Y. Wu, Y.Q. Su, S.J. Ding, C.H.
433 Xiao, Adv. Funct. Mater. 32 (2021) 2107056.
- 434 [25] Z.F. Huang, J.J. Song, K. Li, M. Tahir, Y.T. Wang, L. Pan, L. Wang, X.W. Zhang, J.J. Zou,
435 J. Am. Chem. Soc. 138 (2016) 1359-1365.
- 436 [26] L. Chen, Y.H. Song, Y. Liu, L. Xu, J.Q. Qin, Y.P. Lei, Y.G. Tang, J. Energy Chem. 50 (2020)
437 395-401.
- 438 [27] I.K. Mishra, H. Zhou, J. Sun, F. Qin, K. Dahal, J. Bao, S. Chen, Z. Ren, Energy. Environ. Sci.
439 11 (2018) 2246-2252.
- 440 [28] Y.Y. Song, J.L. Cheng, J. Liu, Q. Ye, X. Gao, J.J. Lu, Y.L. Cheng, Appl. Catal. B Environ.
441 298 (2021) 120488.
- 442 [29] S. Valeri, A. Borghi, G.C. Gazzadi, A. Di Bona, Surf. Sci. 423 (1999) 346-356.
- 443 [30] J. Yu, Q.Q. Li, Y. Li, C.Y. Xu, L. Zhen, V.P. Dravid, J.S. Wu, Adv. Funct. Mater. 26 (2016)
444 7644-7651.
- 445 [31] H.L. Wang, Y. Xie, H.S. Cao, Y.C. Li, L. Li, Z.K. Xu, X.W. Wang, N. Xiong, K. Pan,
446 ChemSusChem 10 (2017) 4899-4908.
- 447 [32] A.P. Grosvenor, M.C. Biesinger, R.S.C. Smart, N.S. McIntyre, Surf. Sci. 600 (2006) 1771-
448 1779.
- 449 [33] S. Yang, J.Y. Zhu, X.N. Chen, M.J. Huang, S.H. Cai, J.Y. Han, J.S. Li, Appl. Catal. B Environ.
450 304 (2022) 120914.
- 451 [34] L.T. Yan, L. Cao, P.C. Dai, X. Gu, D.D. Liu, L.J. Li, Y. Wang, X.B. Zhao, Adv. Funct. Mater.
452 27 (2017) 1703455.
- 453 [35] S. Surendran, S. Shanmugapriya, A. Sivanantham, S. Shanmugam, R. Kalai Selvan, Adv.
454 Energy Mater. 8 (2018) 1800555.

- 455 [36] J. Durst, A. Siebel, C. Simon, F. Hasché, J. Herranz, H.A. Gasteiger, *Energy Environ. Sci.* 7
456 (2014) 2255-2260.
- 457 [37] R. Zhang, X.X. Wang, S.J. Yu, T. Wen, X.W. Zhu, F.X. Yang, X.N. Sun, X.K. Wang, W.P.
458 Hu, *Adv. Mater.* 29 (2017) 1605502.
- 459 [38] C. Zhang, Y.M. Shi, Y.F. Yu, Y.H. Du, B. Zhang, *ACS Catal.* 8 (2018) 8077-8083.
- 460 [39] S.Q. Liu, H.R. Wen, Y. Guo, Y.W. Zhu, X.Z. Fu, R. Sun, C.P. Wong, *Nano Energy* 44 (2018)
461 7-14.
- 462 [40] H.F. Liang, A.N. Gandi, D.H. Anjum, X.B. Wang, U. Schwingenschlögl, H.N. Alshareef,
463 *Nano Lett.* 16 (2016) 7718-7725.
- 464 [41] T. Wang, C. Wang, Y. Jin, A. Sviripa, J. Liang, J. Han, Y. Huang, Q. Li, G. Wu, *J. Mater.*
465 *Chem. A* 5 (2017) 25378-25384.
- 466 [42] W.W. Zou, C.L. Sun, K.N. Zhao, J.T. Li, X.L. Pan, D.X. Ye, Y.P. Xie, W.W. Xu, H.B. Zhao,
467 L. Zhang, J.J. Zhang, *Electrochim. Acta* 345 (2020) 136114.
- 468 [43] S. Anantharaj, S.R. Ede, K. Sakthikumar, K. Karthick, S. Mishra, S. Kundu, *ACS Catal.* 6
469 (2016) 8069-8097.
- 470 [44] Z.Y. Yu, Y. Duan, X.Y. Feng, X.X. Yu, M.R. Gao, S.H. Yu, *Adv. Mater.* 33 (2021) 2007100.
- 471 [45] G. Wu, X.S. Zheng, P.X. Cui, H.Y. Jiang, X.Q. Wang, Y.T. Qu, W.X. Chen, Y. Lin, H. Li, X.
472 Han, Y.M. Hu, P.G. Liu, Q.H. Zhang, J.J. Ge, Y.C. Yao, R.B. Sun, Y. Wu, L. Gu, X. Hong,
473 Y.D. Li, *Nat. Commun.* 10 (2019) 4855.
- 474 [46] J. Wang, L.L. Han, B.L. Huang, Q. Shao, H.L.L. Xin, X.Q. Huang, *Nat. Commun.* 10 (2019)
475 5692.
- 476 [47] Y. Wang, B. Kong, D.Y. Zhao, H.T. Wang, C. Selomulya, *Nano Today* 15 (2017) 26-55.
477

478 **Graphical abstract:**



479
480 Two-dimensional quasi-monolayered NiCoP, synthesized by ultrasonic-cavitation and phase-
481 transition process, can be applied as excellent bifunctional electrocatalyst for overall water splitting.
482

483

Supporting Information

484

485 Long Zhao^a, Ming Wen^{a,*}, Yakun Tian^a, Qingsheng Wu^a, Yongqing Fu^b

486

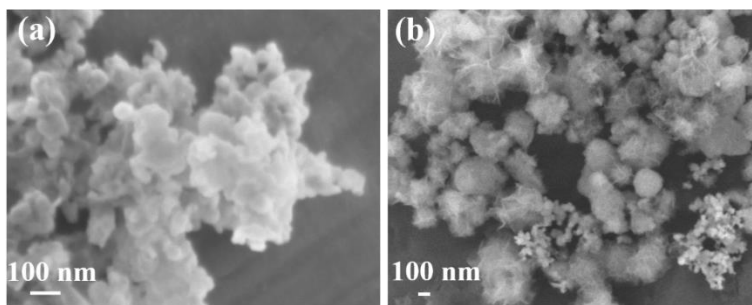
487 ^a *School of Chemical Science and Engineering, Shanghai Key Laboratory of Chemical Assessment*
488 *and Sustainability, State Key Laboratory of Pollution Control and Resource Reuse, Tongji*
489 *University, Shanghai 200092, China*

490 ^b *Faculty of Engineering and Environment, Northumbria University, Newcastle upon Tyne, NE1*
491 *8ST, UK*

492 * Corresponding author. E-mail addresses: m_wen@tongji.edu.cn (M. Wen)

493

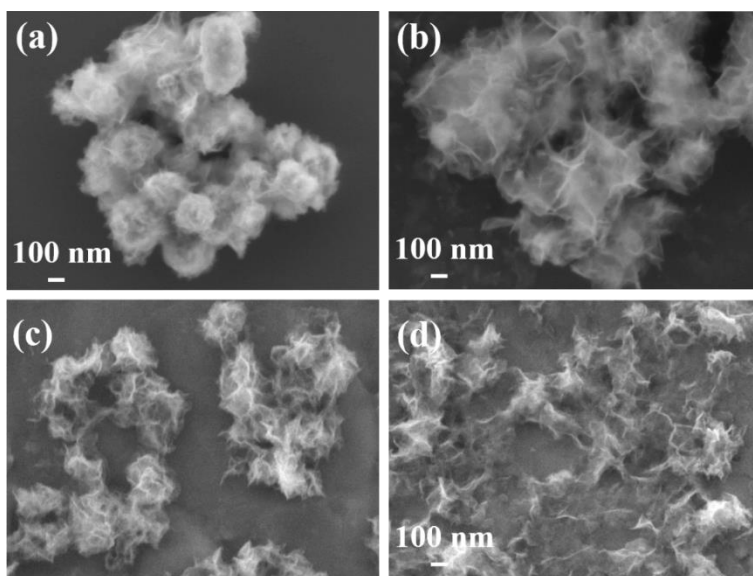
494 **Supporting Figures**



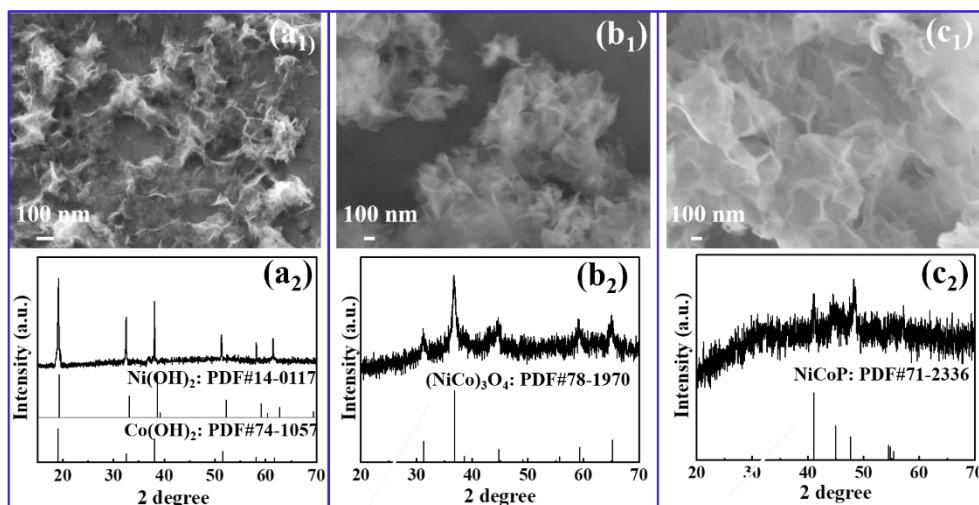
495

496 **Fig. S1.** SEM images of NiCo(OH)₂ obtained by replacing NaBH₄ with NaH (a) and NaOH (b).

497

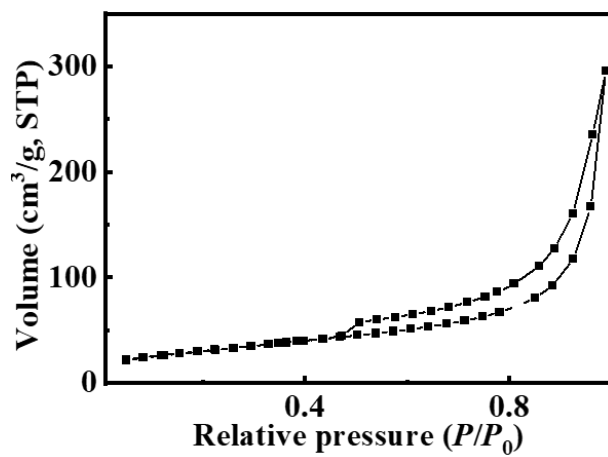


498
499 **Fig. S2.** SEM images of NiCo(OH)₂ precursor obtained at different ultrasonic powers: 0 W (a), 100 W (b), 300
500 W (c), 650 W (d).
501



502
 503 **Fig. S3.** SEM images and XRD patterns for phosphating reaction process: NiCo(OH)₂ (a), (NiCo)₃O₄ (b), NiCoP
 504 (c).

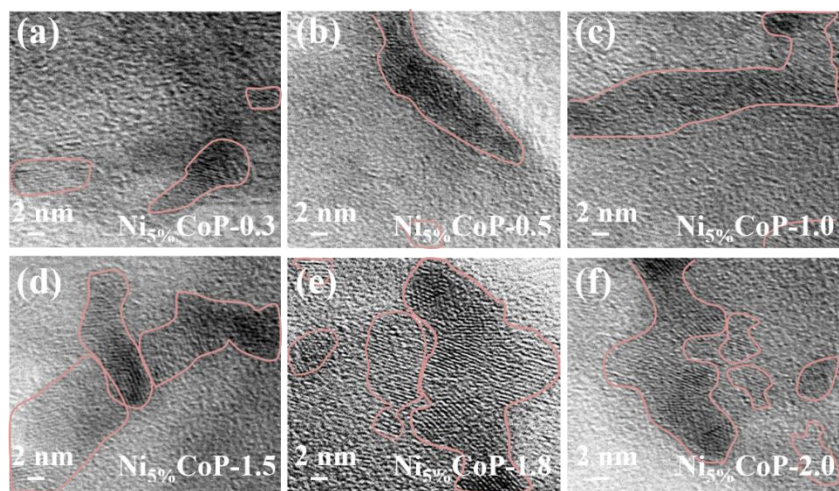
505



506

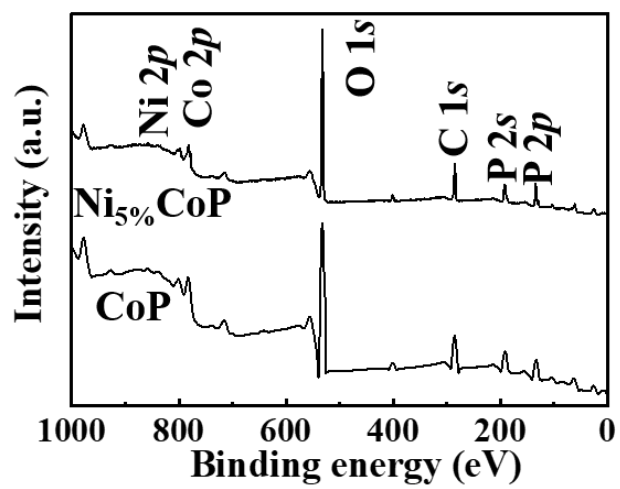
507 **Fig. S4.** The BET result of Ni_{5%}CoP

508



509
510 **Fig. S5.** SEM images of crystalline-amorphous interfaces for samples with different additional amounts of
511 phosphorus.

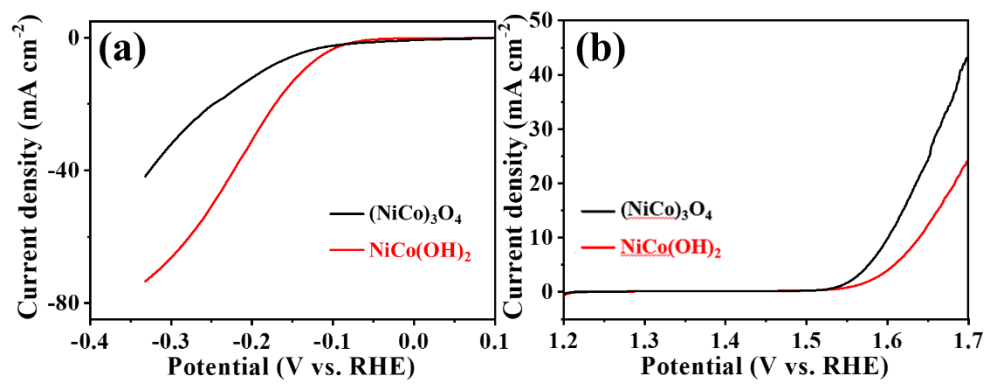
512



513

514 **Fig. S6.** Full XPS survey spectra scans of CoP and Ni_{5%}CoP.

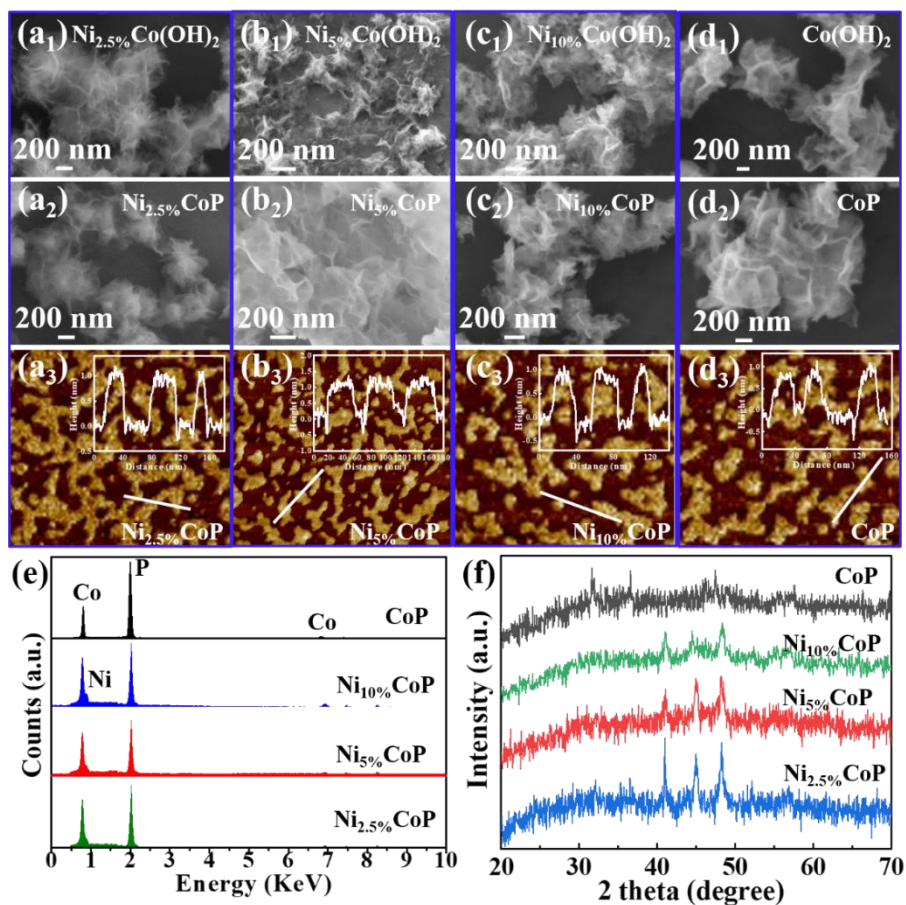
515



516

517 **Fig. S7.** LSV polarization curves of NiCo(OH)₂ and (NiCo)₃O₄ for HER (a) and OER (b).

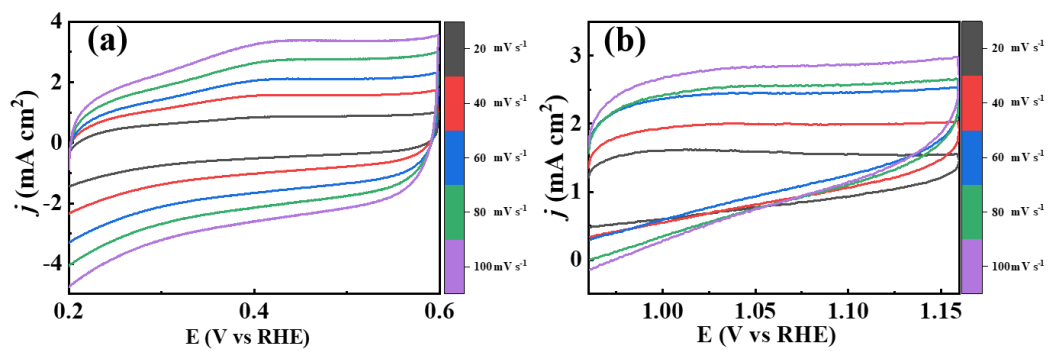
518



519
520 **Fig. S8.** SEM and AFM images (a-d), EDS spectra (e), XRD patterns (f) of NiCoP with different Ni contents.

521 $\text{CoCl}_2 \cdot 6\text{H}_2\text{O}$ (83.3 mg) was dissolved in deionized water (100 mL). Then, 60 mL of this prepared
522 solution was mixed dropwise with a freshly prepared NaBH_4 solution (13 mM, 30 mL) under
523 ultrasonic agitation. After 120 min of reaction, the product of Co(OH)_2 was collected by
524 centrifugation and washed by ethanol and water several times. It was then dried in a freeze drier.
525 Two quartz crucibles were put into a tubular furnace. One was loaded with NaH_2PO_2 (1.8 g) and
526 placed at the upwind side. The other one was loaded with Co(OH)_2 (12 mg) and placed at the
527 downwind side. They were heated up to 350°C (with a heating rate of $2^\circ\text{C} \cdot \text{min}^{-1}$) and kept for 3 h
528 at 350°C for a complete phosphorization. NiCoP were synthesized by a similar protocol of the CoP,
529 except that the starting solutions have dissolved $\text{CoCl}_2 \cdot 6\text{H}_2\text{O}$ (83.3 mg dissolved in 100 mL
530 deionized water, 30 mL) plus $\text{NiCl}_2 \cdot 6\text{H}_2\text{O}$ solution (2.1, 4.2, and 8.3 mg dissolved in 100 mL
531 deionized water respectively, 30 mL). Obtained samples were denoted as $\text{Ni}_{2.5\%}\text{CoP}$, $\text{Ni}_{5.0\%}\text{CoP}$,
532 and $\text{Ni}_{10\%}\text{CoP}$, respectively.

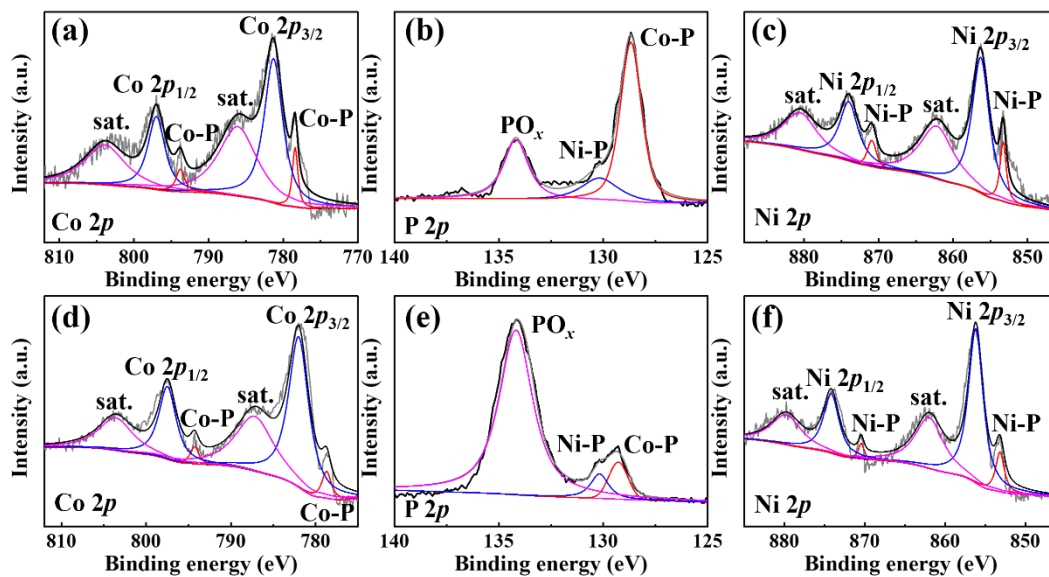
533



534

535 **Fig. S9.** CV curves at various scan rates for HER (a) and OER (b).

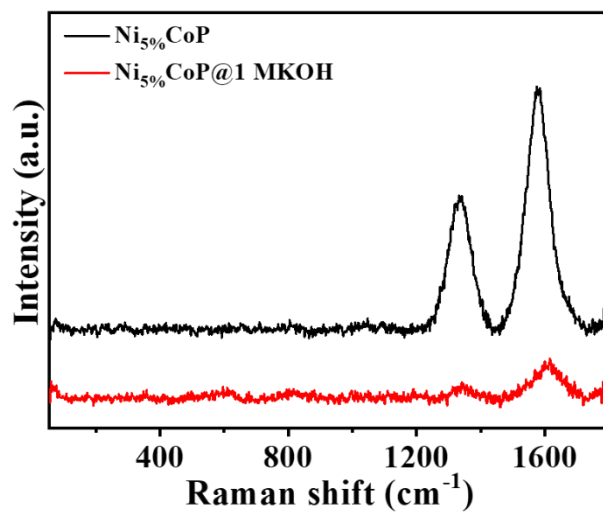
536



537

538 **Fig. S10.** Detail XPS spectra for Co 2p, P 2p, Ni 2p of $\text{Ni}_{5\%}\text{CoP}$ after HER (a-c) and OER (d-f).

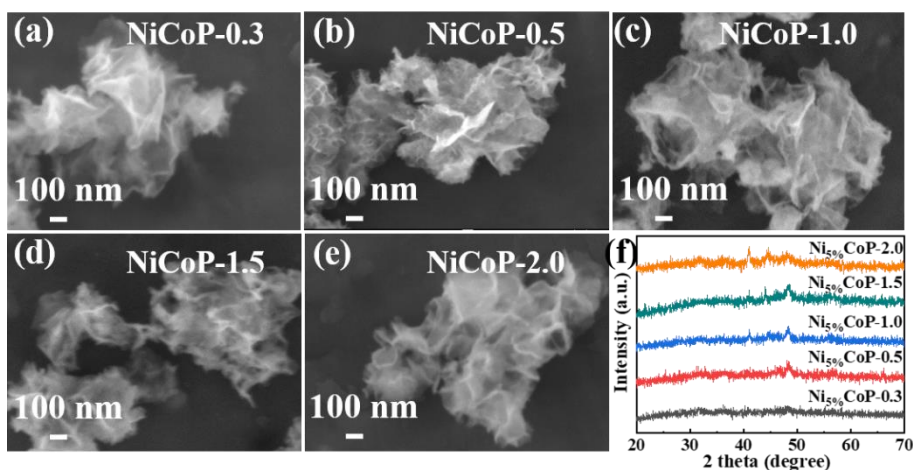
539



540

541 **Fig. S11.** Raman spectra of Ni_{5%}CoP and Ni_{5%}CoP@1 M KOH before overall water splitting

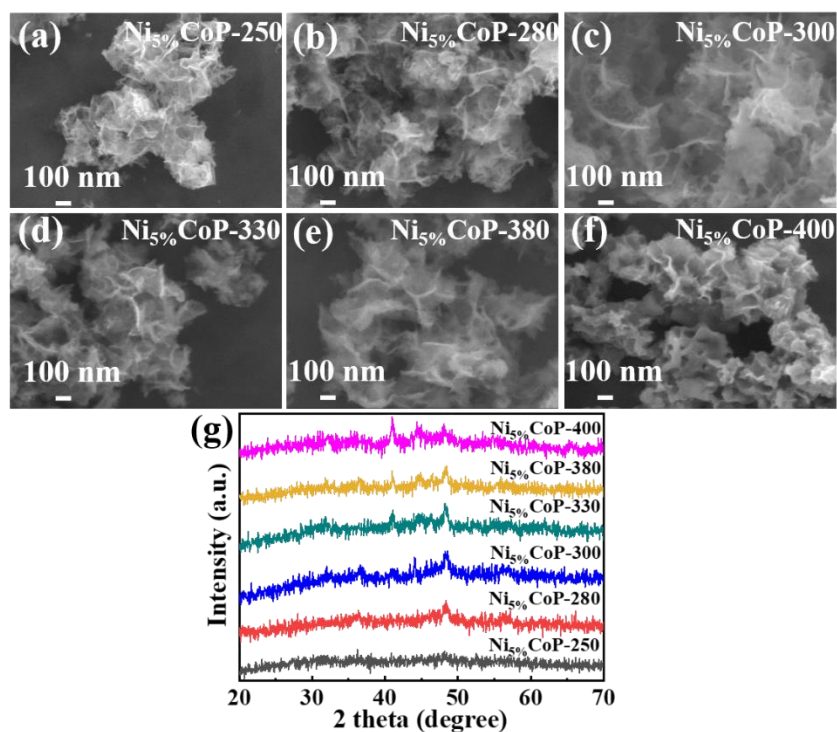
542



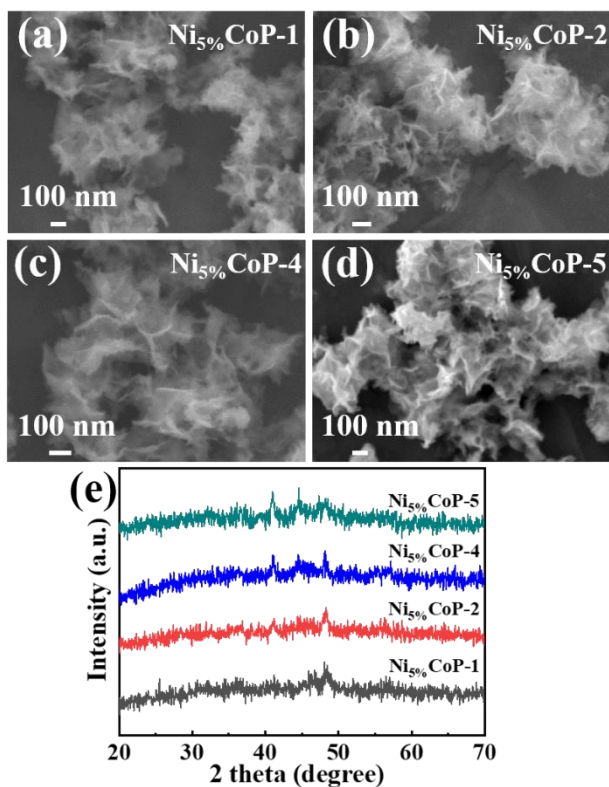
543
 544 **Fig. S12.** SEM images (a-e), XRD patterns (f) of Ni_{5.0%}CoP with different additional amounts of phosphorus.

545 Two quartz crucibles were put into a tubular furnace. One was loaded with Ni_{5.0%}Co(OH)₂ (12
 546 mg) was placed at the downwind side. The other one was loaded with NaH₂PO₂ (0.3 g, 0.5 g, 1.0
 547 g, 1.5 g, 1.8 g, and 2.0 g, respectively) were placed at the upwind side. The furnace temperature
 548 was increased to 350°C with a heating rate of 2°C·min⁻¹ and kept for 3 h at 350°C for the complete
 549 phosphorization. The final products are denoted as Ni_{5.0%}CoP-0.3, Ni_{5.0%}CoP-0.5, Ni_{5.0%}CoP-1.0,
 550 Ni_{5.0%}CoP-1.5, Ni_{5.0%}CoP-1.8, and Ni_{5.0%}CoP-2.0, respectively.

551



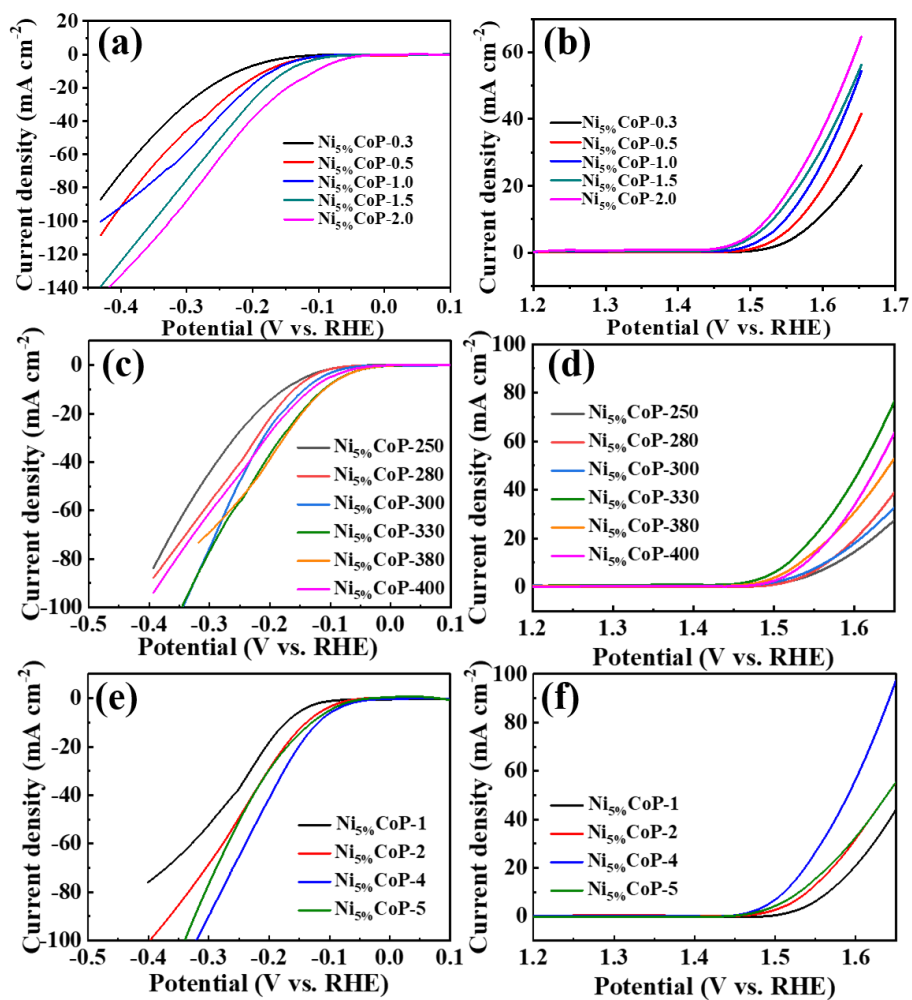
552
 553 **Fig. S13.** SEM images (a-f), XRD patterns (g) of $\text{Ni}_{5.0\%}\text{CoP}$ with different phosphating temperatures.
 554 Two quartz crucibles were put into a tubular furnace. One was loaded with NaH_2PO_2 (1.8 g) was
 555 placed at the upwind side. The other one was loaded with $\text{Ni}_{5.0\%}\text{Co}(\text{OH})_2$ (12 mg) was placed at
 556 the downwind side of tubular furnace. They were heated up to 350°C with a heating rate of
 557 $2^\circ\text{C}\cdot\text{min}^{-1}$ and kept for 3 h at 250°C , 280°C , 300°C , 330°C , 350°C , 380°C , and 400°C for the
 558 complete phosphorization. The final products are denoted as $\text{Ni}_{5.0\%}\text{CoP-250}$, $\text{Ni}_{5.0\%}\text{CoP-280}$,
 559 $\text{Ni}_{5.0\%}\text{CoP-300}$, $\text{Ni}_{5.0\%}\text{CoP-330}$, $\text{Ni}_{5.0\%}\text{CoP-350}$, $\text{Ni}_{5.0\%}\text{CoP-380}$, and $\text{Ni}_{5.0\%}\text{CoP-400}$, respectively.
 560



561
 562 **Fig. S14.** SEM images (a-d), XRD patterns (e) of $\text{Ni}_{5\%}\text{CoP}$ with different phosphating times.

563 Two quartz crucibles were put into a tubular furnace. One was loaded with NaH_2PO_2 (1.8 g) was
 564 placed at the upwind side. The other one was loaded with $\text{Ni}_{5.0\%}\text{Co}(\text{OH})_2$ (12 mg) was placed at
 565 the downwind side of tubular furnace. They were heated to 350°C with a heating rate of $2^\circ\text{C}\cdot\text{min}^{-1}$
 566 and kept for 1 h, 2 h, 3 h, and 4 h for the complete phosphorization. The final products are denoted
 567 as $\text{Ni}_{5.0\%}\text{CoP-1}$, $\text{Ni}_{5.0\%}\text{CoP-2}$, $\text{Ni}_{5.0\%}\text{CoP-3}$, and $\text{Ni}_{5.0\%}\text{CoP-4}$, respectively.

568



569

570 **Fig. S15.** HER and OER performances of Ni₅₀CoP samples under different synthesis conditions

571

572 **Supporting Tables**573 **Table S1.** Comparisons of different catalysts towards HER in a 1 M KOH solution.

Free-standing TMPs-based catalysts				
Materials	Overpotential 10 mA·cm⁻² (mV)	Tafel slope (mV·dec⁻¹)	Current density (mA·cm⁻²)	Reference
Ni _{5%} CoP	84	67	180 (~ 390 mV)	This Work
NiCoP Hierarchical	121	65	150 (~ 325 mV)	1
NiCoP-220 Nanosheets	127	61	40 (~ 190 mV)	2
TMPs-based catalysts with substrates				
Materials	Overpotential 10 mA·cm⁻² (mV)	Tafel slope (mV·dec⁻¹)	Current density (mA·cm⁻²)	Reference
Co-Ni-P@Ti sheets	103	33	200 (~ 170 mV)	3
CoP@CC	209	129	125 (~ 350 mV)	4
FeP@CC	218	146	20 (~ 250 mV)	5
NiSP@NF	68.4	46.6	150 (~ 150 mV)	6
Ni-P nanorods@NF	158	75	300 (~ 300 mV)	7
NiCo phosphide@GO	58	57	150 (~ 150 mV)	8
Fe-CoP HTPAs@ZIF-67	98	69	300 (~ 180 mV)	9
W-CoP NAs@CC	94	63	60 (~ 160 mV)	10
Ni-CoP/HPFs@ZIF-67	92	71	70 (~ 200 mV)	11

574

575 **Table S2.** The weight percentage and atomic percentage of elements in NiCoP with different Ni contents.

Element	Weight (%)	Atomic (%)
CoP		
O	3.21	8.26
P	38.44	51.01
Co	58.35	40.73
Ni _{2.5%} CoP		
O	2.88	7.96
P	28.25	40.32
Co	66.13	49.65
Ni	2.75	2.07
Ni _{5%} CoP		
O	3.08	8.57
P	26.63	38.27
Co	63.01	47.63
Ni	7.29	5.53
Ni _{10%} CoP		
O	3.00	8.31
P	27.39	39.22
Co	57.53	43.33
Ni	12.09	9.14

576

577 **Table S3.** Comparisons of results from different catalysts towards OER in a 1 M KOH solution.

Free-standing TMPs-based catalysts				
Materials	Overpotential 10 mA·cm⁻² (mV)	Tafel slope (mV·dec⁻¹)	Current density (mA·cm⁻²)	Reference
Ni _{5%} CoP	259	46	90 (~ 370 mV)	This Work
Co _{0.8} Fe _{0.2} P	270	50	70 (~ 470 mV)	12
CoNi _(20:1) -P	273	45	50 (~ 295 mV)	13
TMPs-based catalysts with substrates				
Materials	Overpotential 10 mA·cm⁻² (mV)	Tafel slope (mV·dec⁻¹)	Current density (mA·cm⁻²)	Reference
Co-Ni-P@Ti sheets	340	67	500 (~ 470 mV)	3
Ni ₂ P@CP	280	48	300 (~ 570 mV)	14
MoCoP@Co MOF	305	56	100 (~ 370 mV)	15
NiFeP@NPC	350	78	20 (~ 370 mV)	16
Fe-CoP HTPAs@ZIF-67	230	43	300 (~ 270 mV)	9
NiAlP@NF	242	76	75 (~ 470 mV)	17

578

579 **Table S4.** Parameters of mathematical fitting model among P content, phosphating temperature and time, and
 580 relative crystallinity for HER.

Variate	Parameters			
	<i>a</i>	<i>b</i>	<i>c</i>	<i>d</i>
P content	208.31	141.90	-0.5	19.88
	<i>e</i>	<i>f</i>	<i>g</i>	<i>h</i>
	20.55	15.13	0.5	19.88
	<i>i</i>	<i>j</i>	θ	
	20.55	15.54	6.28°	
Phosphating temperature	<i>a</i>	<i>b</i>	<i>c</i>	<i>d</i>
	169.75	84.54	-0.5	347.96
	<i>e</i>	<i>f</i>	<i>g</i>	<i>h</i>
	2.30	37.22	0.5	347.96
	<i>i</i>	<i>j</i>	θ	
	2.30	12.09	0°	
Phosphating time	<i>a</i>	<i>b</i>	<i>c</i>	<i>d</i>
	44.10	112.03	-0.5	118.78
	<i>e</i>	<i>f</i>	<i>g</i>	<i>h</i>
	33.22	62.99	0.5	118.77
	<i>i</i>	<i>j</i>	θ	
	33.22	2.84	0°	

581

582 **Table S5.** Parameters of mathematical fitting model among P content, phosphating temperature and time, and
 583 relative crystallinity for OER.

Variate	Parameters			
	<i>a</i>	<i>b</i>	<i>c</i>	<i>d</i>
P content	392.71	119.99	-0.5	19.84
	<i>e</i>	<i>f</i>	<i>g</i>	<i>h</i>
	9.99	8.83	0.5	19.84
	<i>i</i>	<i>j</i>	θ	
	9.99	8.27	5.45°	
Phosphating temperature	<i>a</i>	<i>b</i>	<i>c</i>	<i>d</i>
	369.97	113.01	-0.5	347.96
	<i>e</i>	<i>f</i>	<i>g</i>	<i>h</i>
	25.69	26.02	0.5	347.96
	<i>i</i>	<i>j</i>	θ	
	25.69	5.74	0°	
Phosphating time	<i>a</i>	<i>b</i>	<i>c</i>	<i>d</i>
	317.62	105.51	-0.5	108.98
	<i>e</i>	<i>f</i>	<i>g</i>	<i>h</i>
	33.22	62.25	0.5	108.98
	<i>i</i>	<i>j</i>	θ	
	33.22	1.58	0°	

584

585 **References**

- 586 [1] X.P. Liu, S.F. Deng, D.D. Xiao, M.X. Gong, J.N. Liang, T.H. Zhao, T. Shen, D.L. Wang, ACS
587 Appl. Mater. Interfaces 11 (2019) 42233-42242.
- 588 [2] X.P. Liu, S.F. Deng, P.F. Liu, J.N. Liang, M.X. Gong, C.L. Lai, Y. Lu, T.H. Zhao, D.L. Wang,
589 Sci. Bull. 64 (2019) 1675-1684.
- 590 [3] Y. Pei, Y. Yang, F.F. Zhang, P. Dong, R. Baines, Y.C. Ge, H. Chu, P.M. Ajayan, J.F. Shen,
591 M.X. Ye, ACS Appl. Mater. Interfaces 9 (2017) 31887-31896.
- 592 [4] J.Q. Tian, Q. Liu, A.M. Asiri, X.P. Sun, J. Am. Chem. Soc. 136 (2014) 7587-7590.
- 593 [5] Y.H. Liang, Q. Liu, A.M. Asiri, X.P. Sun, Y.L. Luo, ACS Catal. 4 (2014) 4065-4069.
- 594 [6] J.J. Duan, S. Chen, C. Zhao, ACS Appl. Mater. Interfaces 10 (2018) 30029-30034.
- 595 [7] J.L. Xing, Z.H. Zou, K.L. Guo, C.L. Xu, J. Mater. Res. 33 (2018) 556-567.
- 596 [8] Z.W. Fang, L.L. Peng, Y.M. Qian, X. Zhang, Y.J. Xie, J.J. Cha, G.H. Yu, J. Am. Chem. Soc.
597 140 (2018) 5241-5247.
- 598 [9] E.L. Hu, J.Q. Ning, D. Zhao, C.Y. Xu, Y.Y. Lin, Y.J. Zhong, Z.Y. Zhang, Y.J. Wang, Y. Hu,
599 Small 14 (2018) 1704233.
- 600 [10] X.Q. Wang, Y.F. Chen, B. Yu, Z.G. Wang, H.Q. Wang, B.C. Sun, W.X. Li, D.X. Yang, W.L.
601 Zhang, Small 15 (2019) 1902613.
- 602 [11] Y. Pan, K. Sun, Y. Lin, X. Cao, Y.S. Cheng, S.J. Liu, L.Y. Zeng, W.C. Cheong, D. Zhao, K.L.
603 Wu, Z. Liu, Y.Q. Liu, D.S. Wang, Q. Peng, C. Chen, Y.D. Li, Nano Energy 56 (2019) 411-
604 419.
- 605 [12] M. Jiang, J. Li, J.M. Li, Y. Zhao, L.J. Pan, Q.Q. Cao, D.H. Wang, Y.W. Du, Nanoscale 11
606 (2019) 9654-9660.
- 607 [13] X.F. Xiao, C.T. He, S.L. Zhao, J. Li, W.S. Lin, Z.K. Yuan, Q. Zhang, S.Y. Wang, L.M. Dai,
608 D.S. Yu, Energy Environ. Sci. 10 (2017) 893-899.
- 609 [14] J.Y. Xu, X.K. Wei, J.D. Costa, J.L. Lado, B. Owens-Baird, L.P.L. Goncalves, S.P.S.
610 Fernandes, M. Heggen, D.Y. Petrovykh, R.E. Dunin-Borkowski, K. Kovnir, Y.V. Kolen'ko,
611 ACS Catal. 7 (2017) 5450-5455.
- 612 [15] C. Guan, W. Xiao, H.J. Wu, X.M. Liu, W.J. Zang, H. Zhang, J. Ding, Y.P. Feng, S.J.
613 Pennycook, J. Wang, Nano Energy 48 (2018) 73-80.
- 614 [16] J. Wang, F. Ciucci, Appl. Catal. B Environ. 254 (2019) 292-299.
- 615 [17] W.R. Cheng, H. Zhang, X. Zhao, H. Su, F.M. Tang, J. Tian, Q.H. Liu, J. Mater. Chem. A 6
616 (2018) 9420-9427.